

Dual-moon forced dynamics and nonlinear aggregation in  
Saturn's F ring: From quasi-periodicity to modulated oscillations

Omar El Deeb\*

*Department of Mathematics, University of Warwick, Coventry, UK*

## Abstract

We develop a minimal nonlinear model to investigate the oscillatory dynamics of Saturn’s F ring under dual-moon forcing from Prometheus and Pandora. The model extends classical predator-prey dynamics by incorporating both a nonlinear mass aggregation term  $kM^n$  and explicit dual-frequency forcing, capturing how higher-order coagulation physics interacts with multi-moon perturbations. Through extensive numerical integration and dynamical systems analysis, including time-series, spectral, stroboscopic mapping, and rotation number diagnostics, we identify distinct dynamical regimes controlled by the parameters  $n$  and  $k$ .

For moderate nonlinearity ( $n = 1.28, k = 0.54$ ), the system exhibits regular quasi-periodic motion on a two-torus, characterized by smooth amplitude modulation and discrete spectral lines. As nonlinearity increases ( $n = 1.30, k = 0.62$ ), the dynamics transition to strongly modulated oscillations with intermittent phase slips, broadened Poincaré bands, and sideband-rich spectra. A rotation number heatmap reveals organized structures in parameter space, with smooth quasi-periodic regions bounded by near-locking bands analogous to Arnold tongues.

Our results demonstrate that the F ring’s complex morphology can emerge from deterministic multi-frequency dynamics rather than stochastic processes, with the system operating near critical boundaries where small parameter variations can trigger macroscopic reorganization. The model provides a framework for understanding pattern formation in other driven granular systems while offering testable predictions for ring observations.

## I. INTRODUCTION

Saturn, the second-largest planet in our solar system, concentrates a remarkable diversity of physical processes in a single system. Its low density, rapid rotation, deep hydrogen–helium atmosphere, powerful magnetosphere, and spectacular rings make it a natural laboratory for planetary physics and celestial mechanics [1, 2]. The system hosts dozens of moons spanning geologic extremes, from Titan’s dense atmosphere to Enceladus’s plumes. Observations across wavelengths reveal active weather, seasonal variability, and ring–moon coupling that continually reshapes the environment [3]. Studying Saturn refines theories of

---

\* omar.el-deeb@warwick.ac.uk

disk dynamics, accretion, and resonance which are key ideas for understanding planetary systems and disks.

The dynamics of Saturn’s rings arise from the interplay of self-gravity, collisions, viscous diffusion, and time-dependent perturbations from embedded and nearby moons. Particles span micron dust to multi-meter aggregates, with optical depth and size distributions varying radially and azimuthally. In this granular disk, inelastic collisions dissipate energy while collective self-gravity promotes transient clumping. Nonlinear processes such as shear reversal and swing amplification can magnify small perturbations [4–6]. Stochastic impacts and meteoroid bombardment inject fine dust, modifying scattering and collisional regimes [7]. Overlapping resonances and variable driving from multiple moons create interference patterns and beats, yielding envelopes in clump amplitude and phase lags between mass buildup and velocity dispersion. This complexity motivates reduced models that capture essential feedback while remaining tractable.

Located near the Roche limit [8], the F ring balances tidal disruption against self-gravity and collisional sticking, making it an ideal setting to study aggregation–fragmentation cycles [9]. Encounters with Prometheus carve channels and trigger dense knots, while Pandora modulates the outer edge, producing quasi-periodic patterns [10, 11]. The ring highlights the sensitivity of granular disks to resonant, time-dependent forcing.

The Cassini–Huygens mission transformed our understanding of Saturn’s system through continuous observation [12, 13]. Cassini’s instruments mapped ring structure at high resolution, tracked temporal variability, and linked features to moon encounters. Imaging revealed multiple F-ring strands, channel formation by Prometheus, knotty clumps, and episodic jets, while stellar occultations constrained particle size distributions and optical depths. Spectroscopy distinguished water-ice signatures and traced dust production. Radar and radio science probed ring mass and microstructure, and gravity measurements refined Saturn’s interior and the moons’ masses. Long-baseline monitoring resolved seasonal effects and synodic recurrences, enabling quantitative links between resonance locations, driving periodicities, and observed morphologies across the ring system.

Early theories of ring origin emphasized catastrophic or collisional scenarios, proposing that rings form from the disruption of a progenitor body or the incomplete accretion of satellite material within the Roche zone. Lumme [14] developed an influential framework linking ring formation to tidal fragmentation and collisional evolution, highlighting how Saturn’s

gravity can inhibit accretion and promote sustained particle populations. Decades later, Canup [15, 16] advanced a comprehensive model in which a Titan-sized satellite migrated inward and experienced mass removal through tidal stripping near Saturn’s Roche limit, naturally generating today’s massive inner rings and potentially seeding the small inner moons.

Despite extensive imaging and theoretical work, a quantitative framework that jointly captures higher-order aggregation physics and dual-moon forcing in the F ring remains underdeveloped. The literature lacks a compact, tractable model that simultaneously integrates a generic nonlinear aggregation law with tunable exponent and amplitude and an explicit two-moon forcing (Prometheus and Pandora). Prior predator-prey models [17] successfully reproduced clumping driven by a single periodic perturber, but typically linearized mass growth or neglected multi-frequency effects [18]. Moreover, several physical mechanisms like gravitational compression, shear reversal, and self-gravity wakes [19–22] can induce nonlinear mass-dependent growth, which a linear term cannot represent. Filling this gap allows us to assess regimes that sustain quasi-periodic stability, predict beat-like envelopes, and connect measurable timescales with the underlying microphysics.

We build on the prior clumping-dispersal framework that tracks two coupled variables (the mean aggregate mass and the square of the relative velocity dispersion) [18, 23] originally analyzed without any explicit two-moon driver. Our contribution is a parsimonious extension that preserves these minimal state variables and the core aggregation-fragmentation physics while introducing a dual driver: Prometheus, anchored to the Cassini-observed synodic cadence, and Pandora, a weaker secondary modulation estimated from mean motions. This addition lets us examine how multifrequency forcing [24] organizes the dynamics without inflating dimensionality or obscuring mechanisms, yielding testable links between observable timescales and interaction strengths. The dual forcing generates rich dynamics including quasi-periodicity, resonant locking, amplitude and phase modulation, and multi-scale transients. We therefore create a coherent platform to analyze beat envelopes, phase lags between mass buildup and velocity dispersion, and the robustness of oscillatory stability under realistic multifrequency perturbations.

The methods of dynamical systems provide a powerful tool that has numerous applications in mathematical and quantitative models [25–30]. In our context, they constitute a principled way to reduce the complex physics of rings into interpretable low-dimensional

models with predictive structure. When multiple frequencies act, quasi-periodicity and beat phenomena emerge, naturally described by tori and secondary bifurcations. Nonlinear parameterizations such as a power-law growth term allow us to embed microphysical effects within a tractable mean-field description and to map regimes where stability is robust to perturbations.

The paper is structured as follows: In Section II, we present the dual-moon forced model. Section III details the resulting dynamics using time-series, spectral, and geometric diagnostics. We also discuss the physical implications of our findings and the limitations of our work in the same section before presenting our conclusions in Section IV.

## II. THE MODEL

The model builds on the clumping-dispersal framework [18, 23] for the clumping dynamics of Saturn’s F ring to account for the combined gravitational perturbations of *Prometheus* and *Pandora*, the inner and outer shepherd moons, respectively. Prometheus’ periodic encounters with the ring’s core are known from Cassini observations to trigger the formation of channels, streamers, and recurrent clumps. Pandora, orbiting just outside the F ring, contributes additional, though weaker, perturbations that modulate the outer edge of the ring and influence its long-term oscillatory stability.

The model describes the coupled evolution of two quantities: the mean aggregate mass  $M(t)$  of the ring particles and the square of their relative velocity dispersion  $V(t)$  (denoted  $X(t)$  in some diagnostic plots; we use  $V$  in the equations). Their temporal behavior arises from coagulation, fragmentation, viscous stirring, and external forcing by the two moons. The nonlinear coagulation term  $kM^n$  phenomenologically represents enhanced aggregation efficiency from microphysical processes such as gravitational instability, shear reversal, and swing amplification [23, 31]. The fragmentation term  $-(V/v_{\text{th}}^2)(M/T)$  accounts for the breakup of aggregates when their relative velocity exceeds the sticking threshold  $v_{\text{th}}$ .

Including the two periodic forcing terms gives the coupled nonlinear system

$$\begin{aligned} \frac{dM}{dt} &= \frac{M}{T} - \frac{V}{v_{\text{th}}^2} \frac{M}{T} + kM^n, \\ \frac{dV}{dt} &= -\frac{(1-\epsilon^2)}{T} V + \frac{M^2}{M_0^2} \frac{v_{\text{esc}}^2}{T_{\text{orb}}} - \left[ A_0 \cos(\omega_1 t) + A_0 \eta \cos(\omega_2 t) \right], \end{aligned} \quad (1)$$

TABLE I. Parameters used for numerical solutions of model (1) with two-moon forcing.

Parameter	Symbol	Value	Description
Orbital period (F ring)	$T_{\text{orb}}$	1	Reference orbital period
Optical depth	$\tau$	0.1	Local optical depth
Collision period	$T = T_{\text{orb}}/(4\tau)$	2.5	Mean collision time
Coefficient of restitution	$\epsilon$	0.6	Collisional dissipation
Reference aggregate mass	$M_0$	$2 \times 10^9$ g	10 m ice clump, $\rho = 0.5$ g cm $^{-3}$
Escape velocity	$v_{\text{esc}}$	0.5 m s $^{-1}$	From surface of $M_0$
Prometheus forcing amplitude	$A_0$	0.1	Forcing magnitude
Pandora relative amplitude	$\eta$	0.25	Forcing amplitude $A_0\eta$
Sticking threshold velocity	$v_{\text{th}}$	1.78	Aggregation threshold
Prometheus forcing period	$T_{s,1}$	$112 T_{\text{orb}}$	Cassini recurrence
Pandora forcing period	$T_{s,2}$	$71 T_{\text{orb}}$	Synodic estimate

where the first cosine term represents the Prometheus forcing and the second, scaled by the dimensionless factor  $\eta \in [0, 1]$ , represents the Pandora forcing.

All times are normalized by the orbital period  $T_{\text{orb}}$  of the F ring (set to unity in the dimensionless system). The physical orbital period at the F-ring core (radius  $a \approx 1.4018 \times 10^5$  km) is

$$T_{\text{orb}} = 2\pi \sqrt{\frac{a^3}{\mu_{\text{Saturn}}}} \approx 0.620 \text{ days.} \quad (2)$$

The synodic period for each moon–ring interaction is determined from their angular velocities:

$$T_{s,i} = \frac{2\pi}{|\Omega_{\text{ring}} - \Omega_i|} = \frac{1}{\left| \frac{1}{T_{\text{ring}}} - \frac{1}{T_i} \right|}, \quad (3)$$

and the corresponding angular frequencies are  $\omega_i = 2\pi/T_{s,i}$ . In practice we adopt

$$T_{s,1} = 112 T_{\text{orb}}, \quad T_{s,2} = 71 T_{\text{orb}}, \quad (4)$$

based on Cassini’s observed Prometheus recurrence [18] and the synodic estimate for Pandora.

*Parameters.* Time is scaled by  $T_{\text{orb}}$ ; the local optical depth  $\tau$  fixes the mean collision time  $T = T_{\text{orb}}/(4\tau)$ , which controls both mass exchange and collisional damping in  $\dot{M}$  and

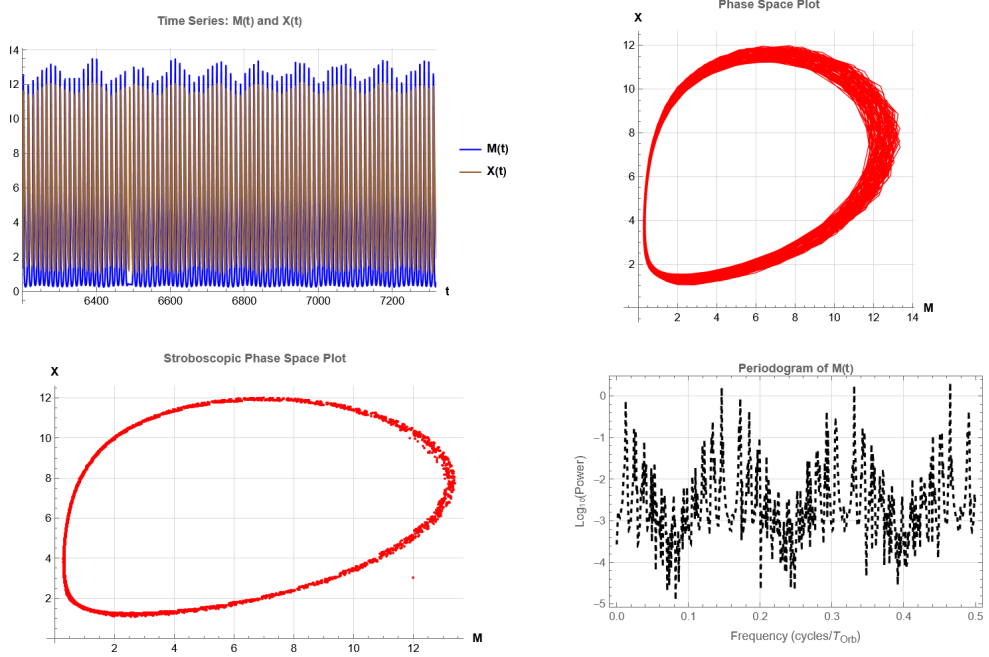


FIG. 1. Upper row: time series and phase portrait over a  $10 T_s$  window. Bottom row: stroboscopic section sampled every  $T_s$  over a very long window ( $10^4 T_S$ ) and a periodogram of  $M(t)$  over  $10 T_s$ . Parameters from Table I with ( $n = 1.30$ ,  $k = 0.62$ ).

$\dot{V}$ . Dissipation in  $\dot{V}$  scales with the coefficient of restitution  $\epsilon$ , while viscous stirring is referenced to the escape-velocity scale  $v_{\text{esc}}$  for an aggregate of mass  $M_0$ . External driving enters  $\dot{V}$  explicitly as  $A_0 \cos(\omega_1 t) + A_0 \eta \cos(\omega_2 t)$  with synodic periods (4). The sticking threshold  $v_{\text{th}}$  sets the velocity beyond which fragmentation dominates aggregation in  $\dot{M}$ . Higher-order aggregation is represented by  $k M^n$ : the exponent  $n > 1$  regulates how rapidly growth accelerates with mass, while  $k \in [0, 1]$  sets the overall intensity of this pathway.

### III. RESULTS AND DISCUSSION

#### A. Time-domain, stroboscopic, and spectral analysis

Figures 1 and 2 characterize the dynamics using four diagnostics: (i) short time series windows of  $M(t)$  and  $X(t)$ ; (ii) the continuous phase portrait  $(M(t), X(t))$ ; (iii) a Poincaré section sampled once every  $T_s$ ; and (iv) a one-sided periodogram of  $M(t)$ . Both figures use identical plotting conventions to enable direct comparison.

Since the forcing is  $T_s$ -periodic, the set  $\{(M(t_k), X(t_k))\}$  with  $t_k = t_0 + k T_s$  defines a

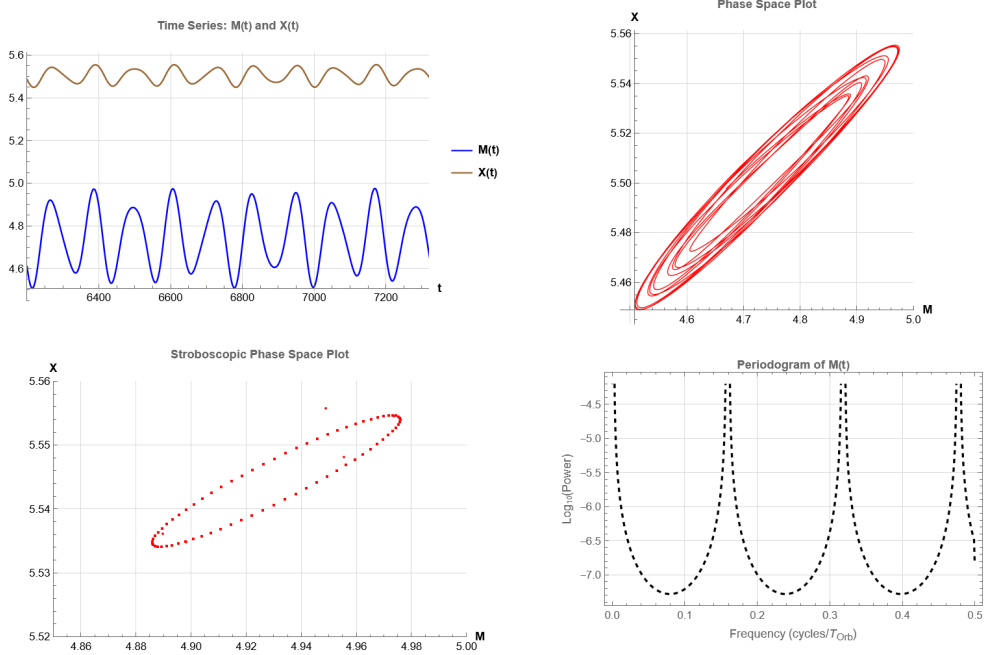


FIG. 2. Same set of diagnostics as Fig. 1. Parameters:  $(n = 1.28, k = 0.54)$ .

Poincaré/stroboscopic map. Its geometry is diagnostically useful: a finite point set indicates frequency locking, a thin closed invariant curve signals quasi-periodicity on a two-torus, while a thickened band or filamented structure indicates strong modulation, phase slips, or weak chaos.

For spectral analysis, we compute periodograms using uniformly sampled  $10 T_s$  windows. After subtracting the sample mean and applying a Blackman–Harris taper to reduce leakage, we scale the discrete Fourier transform by the sampling interval and window power ensuring spectral peaks are comparable across parameter regimes. Narrow isolated peaks indicate coherent oscillations; harmonics and combination tones at  $m/T_s \pm n/T_{s2}$  report nonlinear mixing between the two drives; a broadband floor indicates loss of coherence.

*Figure 1:  $(n = 1.30, k = 0.62)$ .* The  $10 T_s$  time series show highly non-sinusoidal waveforms with sharp pulses and cycle asymmetry, reflecting pronounced nonlinearity. The phase portrait traces a thick, non-elliptic loop with cusp-like features and large radial excursions. The stroboscopic section forms a broad band, indicating persistent modulation and phase-slip behavior with respect to the  $T_s$  drive. The periodogram exhibits numerous spectral lines superimposed on an elevated broadband floor with sidebands around multiples of  $1/T_s$ , characteristic of strong nonlinear mixing between the  $T_s$  and  $T_{s2}$  forcings. Overall, these

signatures are most consistent with modulated oscillations occupying a thick torus.

*Figure 2:* ( $n = 1.28$ ,  $k = 0.54$ ). Here the  $10 T_s$  time series are smooth with only modest amplitude modulation. The phase portrait is nearly elliptical, consistent with motion in a narrow annulus. The stroboscopic section forms a thin closed invariant curve, demonstrating quasi-periodicity on a two-torus. Consistently, the periodogram shows a small number of sharp, well-separated peaks with minimal broadband background.

## B. Unit-circle stroboscopic maps

To complement the preceding analysis, we use *unit-circle stroboscopic maps* to distinguish angular organization from amplitude variability. For each  $(n, k)$  we integrate to  $t_{\max} = 10^6 T_s$ , discard a transient warm-up period, and record strobos at  $t_j = t_0 + jT_s$  to form

$$\mathcal{S} = \{(M(t_j), X(t_j))\}_{j=0}^{N-1}.$$

Under dual incommensurate forcing, this is a Poincaré section with respect to the main forcing. Let  $c = \text{mean}(\mathcal{S})$  and define  $z_j = (M(t_j) - c_M) + i(X(t_j) - c_X)$  with radius  $r_j = |z_j|$  then we project on the unit circle:  $Z_j = z_j/|z_j| = e^{i\theta_j}$ . A uniformly distributed ring indicates a smooth two-frequency torus; azimuthal clustering or partial arcs signal proximity to rational rotation numbers and intermittent phase slips; while pre-projection ring thickening confirms stronger amplitude modulation.

Examining Fig. 3 by rows (fixed  $n$ , increasing  $k$ ) shows two trends. For lower  $n$ , point distributions nearly uniformly cover the circle but with a non-uniform azimuthal density, consistent with the thin invariant curve and discrete, low-noise spectral lines in Fig. 2. As  $n$  increases or  $k$  strengthens, azimuthal inhomogeneity increases, filling the whole circle and the (pre-projection) ring thickens, reflecting the broadened stroboscopic band and sideband-rich spectra of Fig. 1. Thus, the unit-circle diagnostic provides a compact, geometry-based confirmation of the dynamical regime inferred from the time, phase, and spectral views. For larger combinations of  $(n, k)$ , the solutions diverge, resulting in panels labelled “No Solutions” in this grid.

Comparison of the two parameter regimes reveals the transition from strongly nonlinear, multi-frequency dynamics to coherent quasi-periodicity. At  $(n = 1.30, k = 0.62)$  the dynamics show waveform distortion accompanied by a thick Poincaré band with features

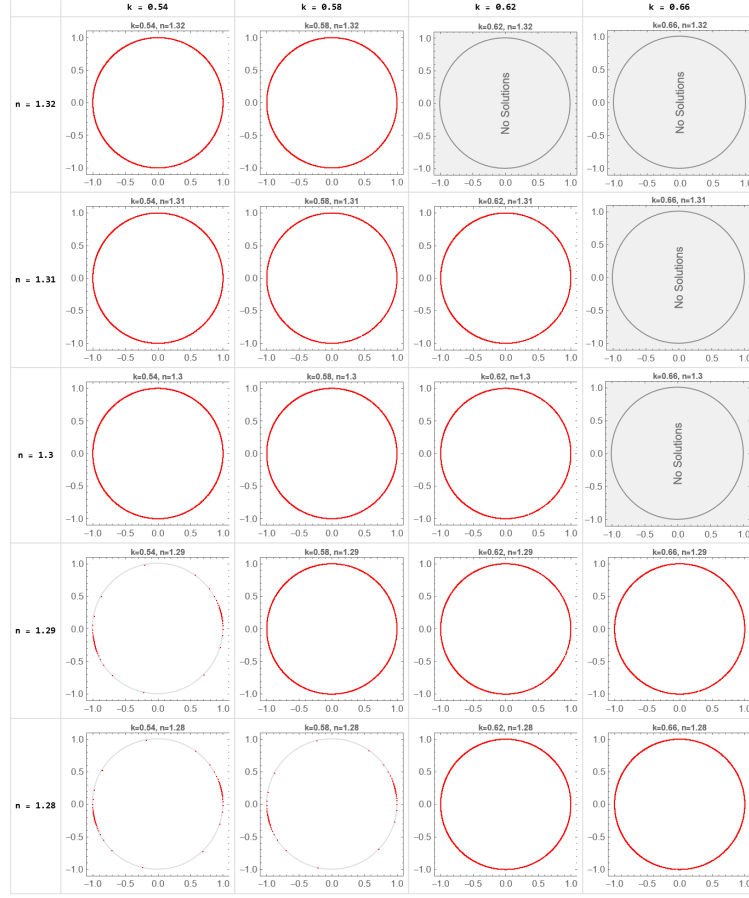


FIG. 3. **Unit-circle stroboscopic maps across  $(n, k)$ .** Each panel shows  $Z_j = z_j/|z_j|$  obtained by centering the stroboscopic samples  $(M(t_j), X(t_j))$ , mapping to the complex plane, and normalizing to the unit circle.

characteristic of modulation and intermittent phase-slip behavior. Decreasing to  $(1.28, 0.54)$  regularizes the dynamics: the Poincaré set becomes a thin invariant circle, exhibiting non-uniform azimuthal point density, consistent with a smooth two-frequency torus.

### C. Stroboscopic radial return maps ( $r_{n+1}$ vs. $r_n$ )

To isolate amplitude dynamics separately of angular organization, we construct a radial return map using the same stroboscopic samples as in Fig. 3. For a given parameter pair  $(n, k)$  we integrate Eq. (1) to a long horizon  $t_{\max} = 10^6 T_s$  after discarding transient warm-up segments, then sample the trajectory once per Prometheus period  $T_s$  at times  $t_j = t_0 + jT_s$ , yielding the set  $\mathcal{S} = \{(M(t_j), X(t_j))\}_{j=0}^{N-1}$ . The point cloud is centered at its centroid

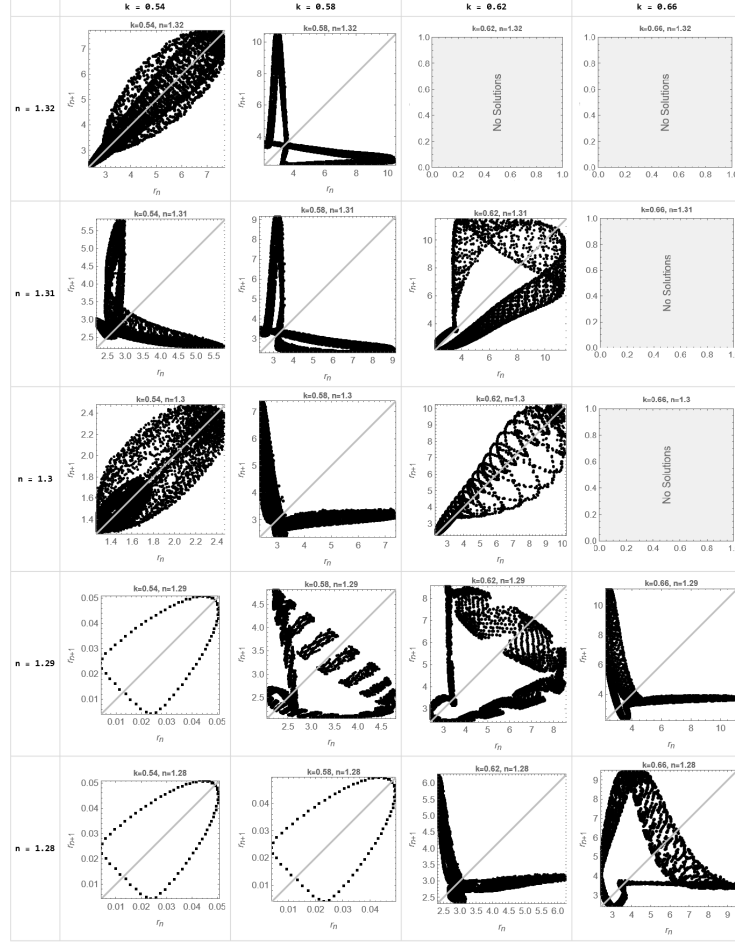


FIG. 4. **Stroboscopic radial return maps across  $(n, k)$ .** Each panel shows the relation between successive stroboscopic radii  $r_n$  and  $r_{n+1}$  computed from centered samples  $(M(t_j), X(t_j))$  taken every  $T_s$ . The gray diagonal is  $r_{n+1} = r_n$ .

$c = (\bar{M}, \bar{X})$  and define complexified, centered points  $z_j = (M(t_j) - \bar{M}) + i(X(t_j) - \bar{X})$ . The stroboscopic radius is

$$r_j = |z_j| = \sqrt{(M(t_j) - \bar{M})^2 + (X(t_j) - \bar{X})^2},$$

which measures distance from the centroid in the  $(M, X)$  plane and thus serves as a scalar measure of the oscillation amplitude at each stroboscopic sample. The radial return map plots the successive-pair relation

$$r_n \mapsto r_{n+1},$$

together with the identity line  $r_{n+1} = r_n$  for reference. Invariant circles with strictly constant radius produce a single point on the diagonal; smooth two-frequency tori with weak am-

plitude modulation collapse to narrow near-diagonal bands; multi-scale modulation, phase slips, or intermittent excursions inflate the cloud off the diagonal and/or produce multi-valued structure. Because the map is one-dimensional in the observable  $r$ , it directly reports how amplitudes transfer from one strobe to the next, complementing the unit-circle map of Fig. 3 that focuses on angle.

The radial return maps in Fig. 4 mirror the progression described on the unit circles of Fig. 3. Tight closed clusters near the diagonal indicate nearly constant stroboscopic radius (coherent two-frequency motion), whereas broadened, structured clouds signal strong amplitude modulation and intermittent excursions consistent with the thick Poincaré bands seen in Figs. 1–3.

For the quasi-periodic regime of Fig. 2 ( $(n, k) = (1.28, 0.54)$ ), the corresponding  $r_{n+1}$  vs.  $r_n$  panel collapses to a tight swarm straddling the diagonal, reflecting an almost constant stroboscopic radius with only weak, smooth amplitude transfer between successive strobes. In other words, the amplitude is slaved to a gentle two-frequency modulation and exhibits no evidence of multi-valued return behavior.

At the nonlinear setting of Fig. 1 ( $(n, k) = (1.3, 0.62)$ ), the radial return panel expands into a visibly thicker cloud about the diagonal, signalling stronger amplitude memory from strobe to strobe and intermittent departures from a quasi-one-dimensional invariant curve. In this regime, the return relation is no longer nearly single-valued: successive amplitudes explore a wider interval, in line with the modulation and phase slips inferred from the other diagnostics.

#### D. Rotation number heatmap:

For each point on a uniformly spaced parameter grid  $(k, n)$  (with  $k \in [0.24, 1.10]$  and  $n \in [1.16, 1.50]$ ), we integrate the dual-forcing system. After discarding initial transients, we sample a stroboscopic set once per Prometheus synodic period  $T_s$ :

$$\mathcal{S} = \{(M(t_j), X(t_j)) : t_j = t_0 + jT_s, j = 0, \dots, N - 1\}.$$

We center  $\mathcal{S}$  at its centroid  $c$  and form the complex, centered sequence

$$z_j = (M(t_j) - c_M) + i(X(t_j) - c_X), \quad r_j = |z_j|.$$

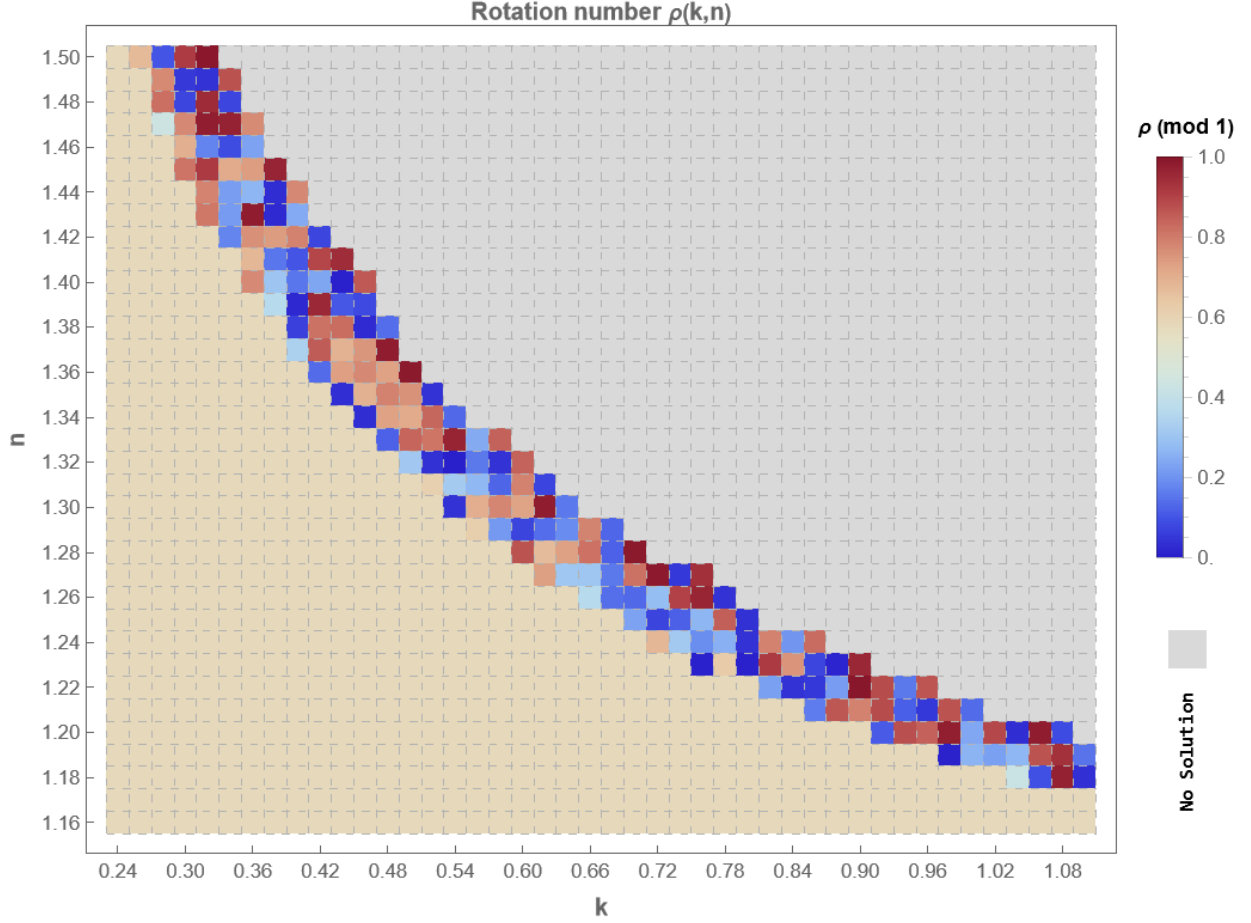


FIG. 5. **Rotation number heatmap over  $(k, n)$ .** Color encodes the stroboscopic rotation number  $\rho(k, n) \bmod 1$  computed from long integrations of the two-moon model; grey cells (“No Solution”) indicate parameter pairs for which reliable stroboscopic sequences could not be obtained. Smooth light orange color variation signals quasi-periodic motion with an incommensurate rotation number, whereas the patches of blue-brown regions indicate near-locking frequencies

The angular increments

$$\Delta\theta_j = \text{wrap}_{(-\pi, \pi]} (\arg z_{j+1} - \arg z_j)$$

define the stroboscopic rotation number

$$\rho(k, n) = \frac{1}{2\pi} \frac{1}{N-1} \sum_j \Delta\theta_j \pmod{1}.$$

We also monitor a standard error of the mean angle increment as an internal diagnostic. Parameter combinations failing reliability checks (too few valid strobos, solver extrapolation

outside tabulated ranges, ...) or yielding divergent solutions are marked as “No Solution” and shaded grey.

The scalar  $\rho(k, n) \bmod 1$  summarizes the mean angular advance of the stroboscopic point cloud per  $T_s$ . Regions with light orange color ( $\rho \simeq 0.50$ ) correspond to quasi-periodic two-frequency motion on a torus: the phase rotates by an almost constant increment each strobe and the cloud lies on a thin invariant loop in  $(M, X)$ . In contrast, in the blue or brown orange regions ( $\rho \simeq 0$  or  $1$ ), the dynamics become strongly nonlinear.

The rotation-number map in Fig. 5 coherently explains the behaviors seen in Figs. 1–2, the unit-circle stroboscopic panels (Fig. 3), and the radial return maps (Fig. 4).

At  $(n=1.28, k=0.54)$  (Fig. 2) the time series are smooth, the stroboscopic set collapses to a thin loop. . In Fig. 5, this point lies in a region of smoothly light orange color. At  $(n=1.3, k=0.62)$  (Fig. 1) the pulses and broadened stroboscopic band indicate strong modulation and proximity to locking. Consistently, Fig. 5 places this point on the blue-brown indicated region.

In analogy with the return map, tight clusters near the diagonal  $r_{n+1} \approx r_n$  indicate weak amplitude modulation and a nearly constant radius of the stroboscopic loop, precisely the quasi-periodic zones of Fig. 5. As  $k$  or  $n$  increase and the heatmap color changes to near-locking, the return clouds broaden, tilt, or form multi-band structures, evidencing stronger amplitude dynamics from cycle to cycle.

## E. Discussions

Our analysis demonstrates that nonlinear mass–velocity coupling under multi-frequency forcing produces self-organized oscillatory states in Saturn’s F ring. By integrating time-domain, spectral, and geometric diagnostics, we establish a consistent physical interpretation: Prometheus acts as the dominant driver sustaining clumping–dispersal cycles, while Pandora introduces slower amplitude modulation that generates quasi-periodic envelopes and intermittent phase-slip behavior. This dynamical duality mirrors the interplay between resonant confinement and weak perturbative diffusion inferred from Cassini observations, indicating that the F ring’s morphological variability may stem from modulation within a precisely tuned nonlinear regime rather than random impacts alone.

Central to the model is the nonlinear aggregation law  $M^n$ , which governs how efficiently

existing clumps capture additional material. When  $n$  exceeds unity, aggregation accelerates faster than linear coagulation, creating a positive feedback where larger aggregates have enhanced collision cross-sections. This leads to superlinear growth that can trigger avalanche-like clumping events. Our numerical diagnostics reveal that increasing  $n$  or the aggregation efficiency  $k$  drives the system from regular two-frequency toroidal motion toward strongly modulated and intermittent states, manifested as broadened Poincaré bands and sideband-rich spectra. Physically, this corresponds to a regime where collisions and self-gravity reinforce moon-driven compression, producing transient over-densities that exceed the fragmentation threshold before relaxing. The alternation between buildup and dispersal constitutes a self-sustained oscillation whose amplitude is governed by the competition between nonlinear growth and dissipative fragmentation.

The appearance of thickened toroidal structures and rotation-number plateaus signifies the emergence of amplitude–phase coupling between the Prometheus and Pandora drives. In planetary terms, this reflects how nearby moons, through their slightly incommensurate synodic frequencies, generate beating patterns that periodically strengthen and weaken the ring’s azimuthal structure. The rotation-number map displays smooth quasi-periodic regions separated by near-locking bands, analogous to Arnold tongues in forced oscillators. Within these tongues, the system momentarily synchronizes to rational frequency ratios between the two drivers, explaining the episodic repetition of bright clumps seen in imaging sequences. Between these tongues, phase drift resumes and the system explores the entire torus, corresponding to the observed alternation between well-defined strands and diffuse textures.

The transition between the representative regimes  $(n, k) = (1.28, 0.54)$  and  $(n, k) = (1.30, 0.62)$  demonstrates remarkable structural instability, where a  $\sim 1.5\%$  variation in  $n$  produces qualitatively different dynamics. The lower parameter pair yields smooth quasi-periodicity, indicating that aggregation and fragmentation remain in balance, while the higher pair leads to pronounced modulation and intermittent excursions characteristic of nonlinear resonance overlap. This sensitivity suggests the F ring operates near a critical threshold, possibly a Hopf bifurcation or Neimark-Sacker transition, where modest variations in moon-ring distance, optical depth, or restitution coefficient could trigger macroscopic reorganization of the entire clumping pattern. The existence of bounded but non-periodic oscillations explains how the F ring maintains long-term coherence without collapsing or

dispersing entirely.

Notably, the model achieves considerable descriptive power with minimal complexity: with only two dynamical variables and a compact set of physically interpretable parameters, it reproduces the main phenomenology of the F ring clump recurrence, envelope modulation, and quasi-stability over thousands of orbital periods. The spectral diagnostics confirm that dual forcing introduces combination tones consistent with nonlinear mixing, while the geometric maps verify that these mixed frequencies correspond to toroidal trajectories in phase space rather than chaotic diffusion. Consequently, the ring’s apparent disorder can be understood as deterministic quasi-periodicity driven by the interplay of nonlinear growth and multi-frequency excitation.

The dynamical regimes we identify, from quasi-periodic tori to modulated oscillations, represent universal responses of nonlinear oscillators to multi-frequency forcing. Our system exhibits behavior analogous to other driven dissipative systems, such as forced Josephson junctions [32, 33], where the interplay between nonlinearity and multiple driving frequencies produces rich synchronization structures. This suggests that the F ring can serve as a natural laboratory for studying general principles of multi-frequency dynamics in astrophysical contexts, with implications for other granular systems subject to multiple periodic perturbations.

## F. Limitations

Although the dual-moon model successfully captures essential dynamical signatures of the F ring, it remains a reduced mean-field representation that omits several layers of physical complexity. The formulation assumes spatial homogeneity and neglects azimuthal phase gradients and stochastic impacts from meteoroid fluxes, which may locally alter collision rates and velocity dispersion. The aggregation–fragmentation law is parameterized phenomenologically, and the exponent  $n$  absorbs multiple microphysical processes that could vary with particle size and composition.

Furthermore, the two-frequency forcing is prescribed deterministically, without feedback from the evolving ring mass distribution onto the moons’ orbital elements and without accounting for time delayed effects. These simplifications enable analytic tractability and clear interpretation of nonlinear responses but limit quantitative comparison with Cassini

imaging and occultation data. Future extensions should embed this reduced model within radially resolved or  $N$ -body frameworks to test the persistence of the observed quasi-periodic regimes under more realistic collisional and gravitational coupling.

#### IV. CONCLUSIONS

Our study develops and analyzes a minimal nonlinear framework that links the micro-physics of aggregation and fragmentation to the macroscopic oscillatory behavior of Saturn’s F ring under dual-moon forcing. By extending the classical predator-prey formulation to include Prometheus and Pandora as distinct periodic drivers, the model provides a dynamical explanation for the principal morphological and dynamical features reported by Cassini-recurrent clumps, envelope modulation, and long-lived braiding. The results demonstrate that the combination of nonlinear aggregation with dual-frequency forcing generates bounded, self-sustained oscillations whose character transitions from regular quasi-periodicity to modulated, near-locking behavior as nonlinear growth strengthens. These dynamics translate physically into alternating episodes of mass concentration and dispersal governed by the beat interaction of the two moons. The identification of distinct dynamical regimes, from coherent quasi-periodicity ( $n = 1.28, k = 0.54$ ) to strongly modulated oscillations ( $n = 1.30, k = 0.62$ ), demonstrates how subtle parameter variations near critical boundaries can produce qualitatively different ring morphologies.

From a broader perspective, the model reveals that the F ring operates near a delicate boundary between stability and resonance overlap, where deterministic modulation replaces randomness as the source of apparent variability. Such positioning endows the system with resilience: perturbations are absorbed through amplitude and phase adjustment rather than catastrophic disruption. Beyond its planetary context, the framework establishes a paradigm for resonance-controlled pattern formation in other driven, dissipative media, from dusty plasmas to accretion disks and granular flows. By combining physical interpretability with dynamical richness, the dual-moon model offers a foundation for future extensions that integrate spatial structure, stochastic perturbations, and observational constraints, thereby deepening our understanding of multi-frequency resonance and oscillatory

stability in complex astrophysical systems.

---

- [1] Colwell, J. E. and Nicholson, P. D. and Tiscareno, M. S. and Murray, C. D. and French, R. G. and Marouf, E. A. (2009) The Structure of Saturn's Rings. *Saturn from Cassini-Huygens* 375–412 doi: 10.1007/978-1-4020-9217-6-13
- [2] Cook, A.F. and Franklin, F.A. and Palluconi, F.D. (1973) Saturn's rings—A survey. *Icarus* **18** 317–337 doi: 10.1016/0019-1035(73)90214-5
- [3] Blanc, Michel and Crida, Aurélien and Shibaike, Yuhito and Charnoz, Sébastien and El Moutamid, Maryame and Estrada, Paul and Mousis, Olivier and Salmon, Julien and Schneebberger, Antoine and Vernazza, Pierre (2025) Understanding the Formation of Saturn's Regular Moons in the Context of Giant Planet Moons Formation Scenarios. *Space Science Reviews* **221** 35 doi: 10.1007/s11214-025-01156-8
- [4] Cuzzi, J. N. and Burns, J. A. and Charnoz, S. and Clark, R. N. and Colwell, J. E. and Dones, L. and Esposito, L. W. and Filacchione, G. and French, R. G. and Hedman, M. M. and Kempf, S. and Marouf, E. A. and Murray, C. D. and Nicholson, P. D. and Porco, C. C. and Schmidt, J. and Showalter, M. R. and Spilker, L. J. and Spitale, J. N. and Srama, R. and Sremčević, M. and Tiscareno, M. S. and Weiss, J. (2010) An Evolving View of Saturn's Dynamic Rings. *Science* **327** 1470–1475 doi: 10.1126/science.1179118
- [5] Cuzzi, J. N. and Whizin, A. D. and Hogan, R. C. and Dobrovolskis, A. R. and Dones, L. and Showalter, M. R. and Colwell, J. E. and Scargle, J. D. (2014) Saturn's F Ring core: Calm in the midst of chaos. *Icarus* **232** 157–175 doi: 10.1016/j.icarus.2013.12.027
- [6] Tajeddine, Radwan and Nicholson, Philip D. and Longaretti, Pierre-Yves and Moutamid, Maryame El and Burns, Joseph A. (2017) What Confines the Rings of Saturn?. *The Astrophysical Journal Supplement Series* **232** 28 doi: 10.3847/1538-4365/aa8c09
- [7] Rein, H. and Papaloizou, J. C. B. (2010) Stochastic orbital migration of small bodies in Saturn's rings. *Astronomy & Astrophysics* **524** A22 doi: 10.1051/0004-6361/201015177
- [8] Williams, I. P. (2003) The Roche Limit. *Celestial Mechanics and Dynamical Astronomy* **87** 13–25 doi: 10.1023/A:1026137401540
- [9] Brilliantov, N. V. and Otieno, W. and Matveev, S. A. and Smirnov, A. P. and Tyrtyshnikov, E. E. and Krapivsky, P. L. (2018) Steady oscillations in aggregation-fragmentation processes.

*Physical Review E* **98** 012109 doi: 10.1103/PhysRevE.98.012109

- [10] Farmer, Alison J. and Goldreich, Peter (2006) Understanding the behavior of Prometheus and Pandora. *Icarus* **180** 403–411 doi: 10.1016/j.icarus.2005.10.005
- [11] Poulet, F. and Sicardy, B. (2001) Dynamical evolution of the Prometheus–Pandora system. *Monthly Notices of the Royal Astronomical Society* **322** 343–355 doi: 10.1046/j.1365-8711.2001.04128.x
- [12] Ingersoll, Andrew P. (2020) Cassini Exploration of the Planet Saturn: A Comprehensive Review. *Space Science Reviews* **216** 122 doi: 10.1007/s11214-020-00751-1
- [13] Spilker, Linda (2019) Cassini–Huygens’ exploration of the Saturn system: 13 years of discovery. *Science* **364** 1046–1051 doi: 10.1126/science.aat3760
- [14] Lumme, Kari (1972) On the formation of Saturn’s rings. *Astrophysics and Space Science* **15** 404–414 doi: 10.1007/BF00649769
- [15] Charnoz, S. and Canup, R. M. and Crida, A. and Dones, L. (2018) The Origin of Planetary Ring Systems. *Planetary Ring Systems: Properties, Structure, and Evolution* 517–538 doi: 10.1017/9781316286791.018
- [16] Canup, Robin M. (2010) Origin of Saturn’s rings and inner moons by mass removal from a lost Titan-sized satellite. *Nature* **468** 943–946 doi: 10.1038/nature09661
- [17] Diz-Pita, Érika and Otero-Espinar, M. Victoria (2021) Predator–Prey Models: A Review of Some Recent Advances. *Mathematics* **9** 1783 doi: 10.3390/math9151783
- [18] Esposito, Larry W. and Albers, Nicole and Meinke, Bonnie K. and Sremčević, Miodrag and Madhusudhanan, Prasanna and Colwell, Joshua E. and Jerousek, Richard G. (2012) A predator–prey model for moon-triggered clumping in Saturn’s rings. *Icarus* **217** 103–114 doi: 10.1016/j.icarus.2011.09.029
- [19] Tiscareno, Matthew S. and Perrine, Randall P. and Richardson, Derek C. and Hedman, Matthew M. and Weiss, John W. and Porco, Carolyn C. and Burns, Joseph A. (2010) AN ANALYTIC PARAMETERIZATION OF SELF-GRAVITY WAKES IN SATURN’S RINGS, WITH APPLICATION TO OCCULTATIONS AND PROPELLERS. *The Astronomical Journal* **139** 492–503 doi: 10.1088/0004-6256/139/2/492
- [20] Colwell, J. E. and Esposito, L. W. and Sremčević, M. and Stewart, G. R. and McClintock, W. E. (2007) Self-gravity wakes and radial structure of Saturn’s B ring. *Icarus* **190** 127–144 doi: 10.1016/j.icarus.2007.03.018

[21] Nicholson, P. D. and Hedman, M. M. (2010) Self-gravity wake parameters in Saturn's A and B rings. *Icarus* **206** 410–423 doi: 10.1016/j.icarus.2009.07.028

[22] Ghigliotti, Giovanni and Lobry, Laurent and Gallier, Stany and Blanc, Frédéric and Lemaire, Elisabeth and Peters, François (2015) Shear-reversal in non-Brownian suspensions : experiments and simulations. *SoftComp Topical Workshop: Dense Suspension Flow* URL: <https://hal.science/hal-01171413>

[23] El Deeb, Omar (2024) Higher order mass aggregation terms in a nonlinear predator-prey model maintain limit cycle stability in Saturn's F ring. *Physica D: Nonlinear Phenomena* **468** 134311 doi: 10.1016/j.physd.2024.134311

[24] Nayfeh, Ali H. and Mook, Dean T. (2024) Nonlinear Oscillations. *John Wiley & Sons*

[25] Li, Yang and Duan, Jinqiao (2021) A data-driven approach for discovering stochastic dynamical systems with non-Gaussian Lévy noise. *Physica D: Nonlinear Phenomena* **417** 132830 doi: 10.1016/j.physd.2020.132830

[26] Hamzi, Boumediene and Owhadi, Houman (2021) Learning dynamical systems from data: A simple cross-validation perspective, part I: Parametric kernel flows. *Physica D: Nonlinear Phenomena* **421** 132817 doi: 10.1016/j.physd.2020.132817

[27] Massar, Serge (2025) Equilibrium propagation for learning in Lagrangian dynamical systems. *Physical Review E* **112** 035304 doi: 10.1103/smt9-1t11

[28] Gotoda, Hiroshi and Shinoda, Yuta and Kobayashi, Masaki and Okuno, Yuta and Tachibana, Shigeru (2014) Detection and control of combustion instability based on the concept of dynamical system theory. *Physical Review E* **89** 022910 doi: 10.1103/PhysRevE.89.022910

[29] Huang, Liang and Chen, Qingfei and Lai, Ying-Cheng and Pecora, Louis M. (2009) Generic behavior of master-stability functions in coupled nonlinear dynamical systems. *Physical Review E* **80** 036204 doi: 10.1103/PhysRevE.80.036204

[30] Dibeh, Ghassan and El Deeb, Omar (2024) Synchronization and limit cycles in a simple contagion model with time delays. *Physica D: Nonlinear Phenomena* **470** 134417 doi: 10.1016/j.physd.2024.134417

[31] Ross, A. E. and McKenzie, D. R. (2016) Predator-prey dynamics stabilised by nonlinearity explain oscillations in dust-forming plasmas. *Scientific Reports* **6** 24040 doi: 10.1038/srep24040

[32] Baxevanis, G. and Hizanidis, J. (2025) Inductively coupled Josephson junctions: A platform for rich neuromorphic dynamics. *Physical Review E* **111** 044214 doi: 10.1103/Phys-

[33] Meister, S. and Mecklenburg, M. and Gramich, V. and Stockburger, J. T. and Ankerhold, J. and Kubala, B. (2015) Resonators coupled to voltage-biased Josephson junctions: From linear response to strongly driven nonlinear oscillations. *Physical Review B* **92** 174532 doi: 10.1103/PhysRevB.92.174532